Black phosphorus phase retarder based on anisotropic refractive index dispersion

To cite this article: Seong-Yeon Lee and Ki-Ju Yee 2022 *2D Mater.* **9** 015020

2D Materials

PAPER

RECEIVED
1 September 2021

REVISED
13 November 2021

ACCEPTED FOR PUBLICATION
17 November 2021

PUBLISHED
30 November 2021

Black phosphorus phase retarder based on anisotropic refractive index dispersion

Seong-Yeon Lee and Ki-Ju Yee*

Department of Physics and Institute of Quantum Systems, Chungnam National University, Daejeon 34134, Republic of Korea
* Author to whom any correspondence should be addressed.

E-mail: kyee@cnu.ac.kr

Keywords: 2D phase retarder, black phosphorus, anisotropic refractive index dispersion, linear dichroism

Supplementary material for this article is available online

Abstract

Black phosphorus (BP) has gained wide interest as a promising layered material for its unique physical properties. In particular, the anisotropic optical property of BP can act as a retarder or a polarizer in nano-optoelectronic devices, for which quantitative qualification of the phase retardation and the anisotropic refractive index dispersion are essential. Here, we report the anisotropic refractive index and extinction coefficient dispersions of BP in the visible and near infrared range of 540–1500 nm, and then characterize optical phase retardation in a BP flake. Cauchy absorbent equations are provided for the refractive index dispersions along both armchair and zigzag directions, which well reproduce the experimentally measured reflectance and transmittance contrast spectra of BP flakes. Furthermore, we demonstrate that a linear polarized light through BP becomes elliptical, a finding that agrees well with simulation results using the obtained anisotropic refractive index dispersions. The two-dimensional phase retarder in this work is expected to find various applications in novel polarization-sensitive nano-optoelectronic devices.

1. Introduction

In recent decades, two-dimensional (2D) materials like graphene, hexagonal boron nitride, and transition metal dichalcogenides (TMDCs) have been extensively studied [1–6]. Among them, black phosphorus (BP) has gained great interest due to its outstanding characteristics such as high carrier mobility, layer number tuned direct bandgap, and anisotropic material properties [7–14]. In particular, the crystal orientation sensitive nature of BP's electrical, mechanical, thermoelectric, and optical properties has been intensively investigated and has led to novel nano-optoelectrical applications [15].

Black phosphorus has an anisotropically large absorption coefficient along the armchair (AC) axis, and this linear dichroism has been utilized as a linear polarizer [16, 17]. On the other hand, the relatively less studied birefringence of BP is believed to have the potential to be developed as an optical phase retarder or a circular polarizer. In TMDCs such as MoS_2 and WSe_2, specific valleys can be excited by a circularly polarized light [18, 19]; thus, the birefringence of BP can be leveraged for the valley-selective excitation of TMDCs, such that BP/TMDC heterostructures may provide good platforms for valley creation in valleytronics. In this regard, accurately characterizing the anisotropic refractive index dispersion of BP and demonstrating the optical phase retardation are essential.

Several works have reported experimental or theoretical estimations of the anisotropic refractive indices of BP, but to date, the results are rather scattered and await more reliable quantification [8, 20–22]. For example, Wang *et al* reported $n_{AC} = 2.63$ and $n_{ZZ} = 2.71$ for the refractive indices along the AC and zigzag (ZZ) directions at 532 nm, while Mao *et al* reported $n_{AC} = 3.04$ and $n_{ZZ} = 3.20$ [8, 20]. In addition, Schuster *et al* gave a negative value of $\Delta n = n_{ZZ} - n_{AC} \approx -0.2$ in the wavelength range of 540–1500 nm, but according to Jiang *et al*, the birefringence of BP at 532 nm is positive with $\Delta n \approx 0.27$ [21, 22].

In this paper, we first acquire the complex refractive indices of BP from the transfer matrix method (TMM) analysis of experimentally measured

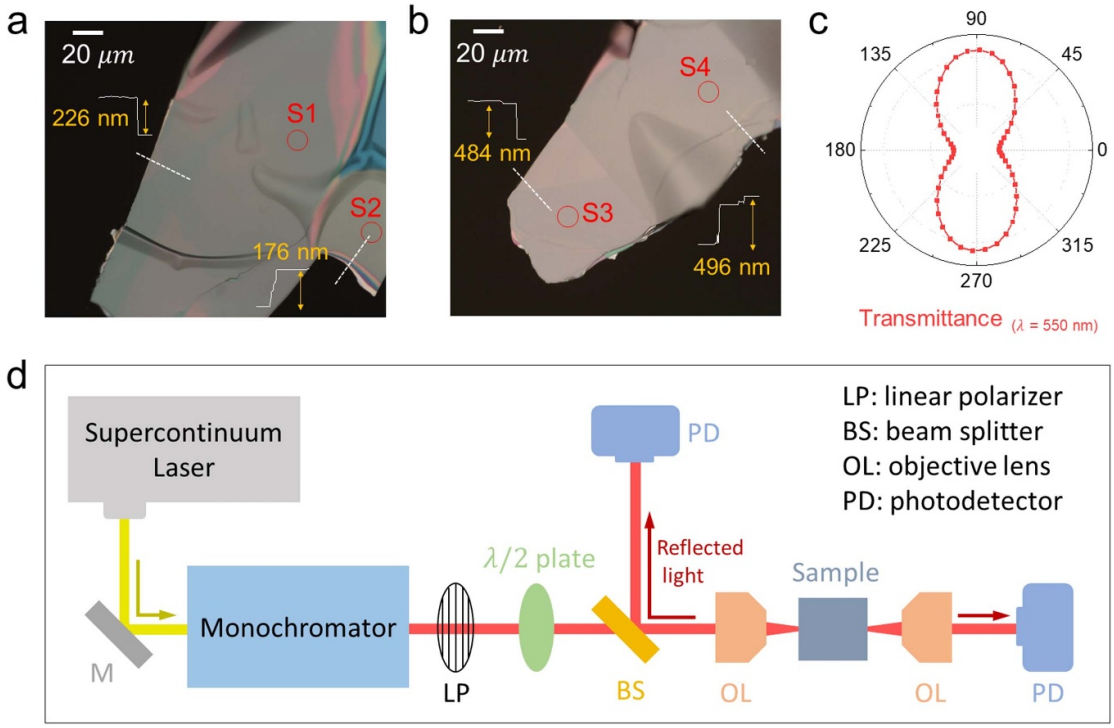

Figure 1. (a), (b) Optical microscope images of BP flakes and sectional height profiles obtained by an atomic force microscope. The areas where the reflectance and transmittance measurements were taken are indicated with red circles and labelled S1–S4. The height profiles were taken across the white dashed lines. (c) Polar plot of the polarization-dependent transmittance at S1 at a wavelength of 550 nm. (d) Schematic of the experimental setup for the simultaneous reflectance and transmittance measurements. A linear polarizer and half-wave plate are used to rotate the linear polarization.

reflectance contrast (RC) and transmittance contrast (TC) spectra. The refractive indices in the visible and near infrared region of 540–1500 nm are modelled with the Cauchy absorbent equations for both AC and ZZ polarizations. We then reveal that a linear polarization passing through a BP flake becomes elliptically polarized as a result of the anisotropic complex refractive index, and that the degree of polarization (DOP) strongly depends on the input polarization angle as well as the BP sample thickness and wavelength. We successfully reproduce this optical phase retardation and corresponding DOP spectrum via TMM simulation, and find that multiple reflections at BP interfaces induce the observed sinusoidal wavelength dependence.

2. Methods

2.1. Sample preparation

We mechanically exfoliated BP flakes using sticky tape from a bulk crystal and transferred them onto transparent fused silica (FS) substrates [23, 24]. Optical images of two such flakes are shown in figures 1(a) and (b), where the relatively flat regions denoted by S1 to S4 were selected for further optical investigations. The sample thicknesses at the spots were acquired *a priori* from the sectional surface profiles using atomic force microscopy (see section 1 in the supporting information available online at stacks.iop.org/2DM/9/015020/mmedia). In order to prevent surface degradation under ambient atmosphere, the BP samples were kept and measured under vacuum conditions. Figure 1(c) shows a polar plot of the transmittance as a function of light polarization at 550 nm for the spot S1 with an estimated thickness of 226 nm. Because of the strong anisotropy of the light absorption, the two principal axes of BP crystal, the AC and *ZZ* directions, were confirmed by the light polarization of the minimum and maximum transmittance, respectively.

2.2. Experimental setup

In order to obtain the anisotropic refractive index and absorption coefficient of BP, we simultaneously measured the polarization-sensitive RC and TC spectra over the spectral range of 540–1500 nm. The experimental setup is shown in figure 1(d). We used a supercontinuum light source (SuperK compact, NKT Photonics) for measuring the RC and TC spectra simultaneously. The broad band light was spectrally filtered by a monochromator (DK240, CVI), and was incident on the sample after passing through a beam splitter and an objective lens (M Plan Apo NIR ×20, Mitutoyo). The reflected and transmitted light intensity was measured with a Si photodiode at the visible wavelengths and a Ge photodiode at the near infrared wavelengths. Linear light polarization was changed by rotating a half-wave plate located after a linear polarizer. The intensities reflected and transmitted

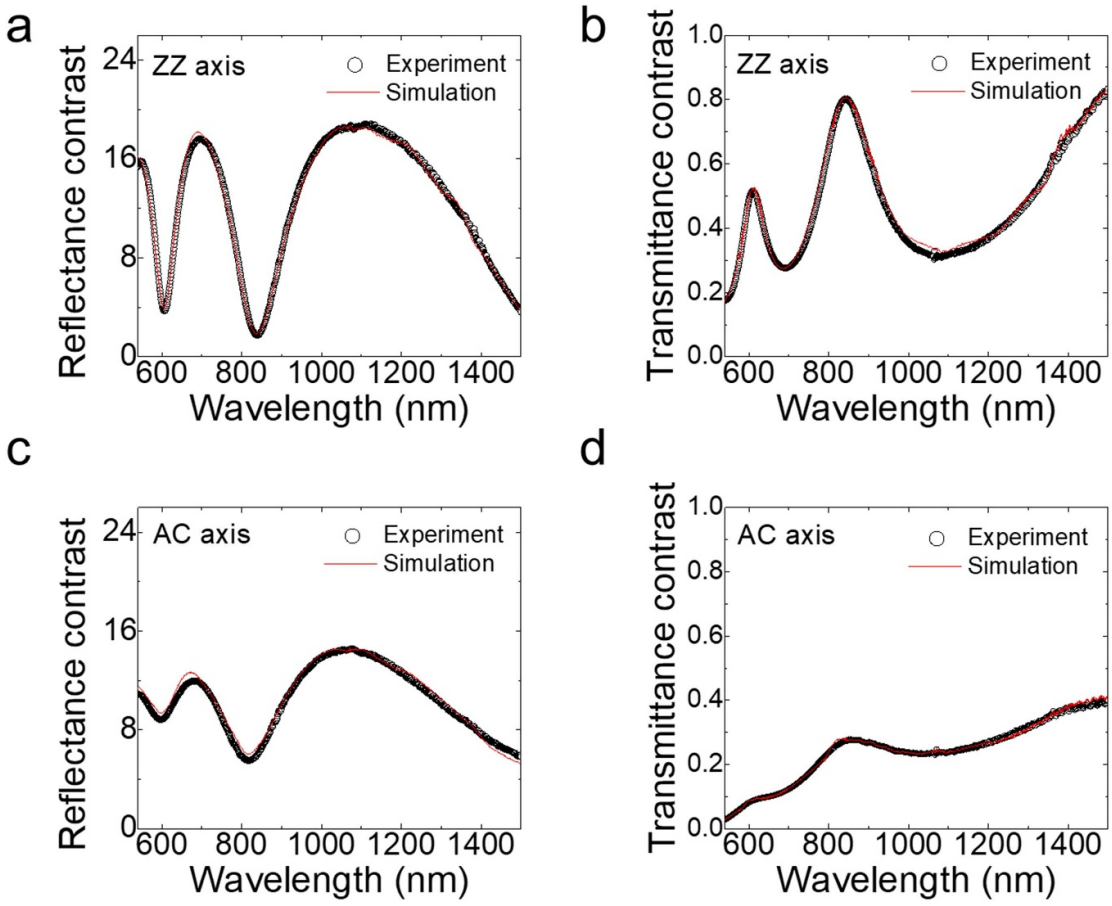

Figure 2. (a), (b) Measured (black circles) and simulated (red lines) reflectance and transmittance contrast spectra for a 226 nm thick BP flake with the ZZ axis polarization. (c), (d) Those with the AC axis polarization. The refractive index and extinction coefficient dispersions used in the simulations are given with dashed lines in figure 3(a) and (b).

both at the BP flake and at the FS substrate were measured, with RC (TC) defined as the reflected (transmitted) intensity ratio at the BP flake relative to that at the FS substrate.

3. Results and discussion

We first discuss the polarization-sensitive RC and TC spectra at the spot S1 in figure 1(a). Figures 2(a) and (b) show the RC and TC spectra for the ZZ polarization, respectively, and figures 2(c) and (d) display those for the AC polarization, respectively. Here, RC is greater than one because the reflectance is stronger at BP than at the FS substrate. The fact that the TC of the AC polarization is much smaller than that of the ZZ polarization indicates a large linear dichroism of BP. All the RC and TC spectra exhibit spectral modulations from thin film interference between the light reflected at the BP interfaces, where the modulation period depends on the refractive index and the flake thickness.

We find in figures 2(c) and (d) that the modulation depth is smaller for the AC polarization because of severe attenuation of propagating light through a BP flake along this axis. As the BP thickness decreases, the wavelength separation between adjacent maxima in the RC or TC spectrum becomes larger (see section 2 in the supporting information). We note that the overall strength of the RC as well as the modulation period can provide a rough estimate of the refractive index (see section 3 in the supporting information).

From the acquired RC and TC values at each wavelength, the real and imaginary components of the complex refractive index of BP can be extracted by applying TMM analysis inversely [25, 26]. Under the TMM approach, the electric field amplitudes at the FS region (A_4, B_4) can be calculated by multiplying a 2 × 2 transfer matrix (M) to the field amplitudes of air (A_1, B_1). As the refractive index of fused silica (n_{fs}) is well known, the matrix M is a function of the complex refractive index ($\tilde{n}$) and thickness L of BP. Inversely applying the TMM, the RC and TC values convert to the corresponding complex refractive index of BP (see section 4 in the supporting information). As shown in figures 2(a)–(d) for spot S1 and in section 2 in the supporting information for other spots S2–S4, we determined the complex refractive index dispersions, which well reproduce the experimental RC and TC spectra at each spot. The refractive index (n) and extinction coefficient (κ)

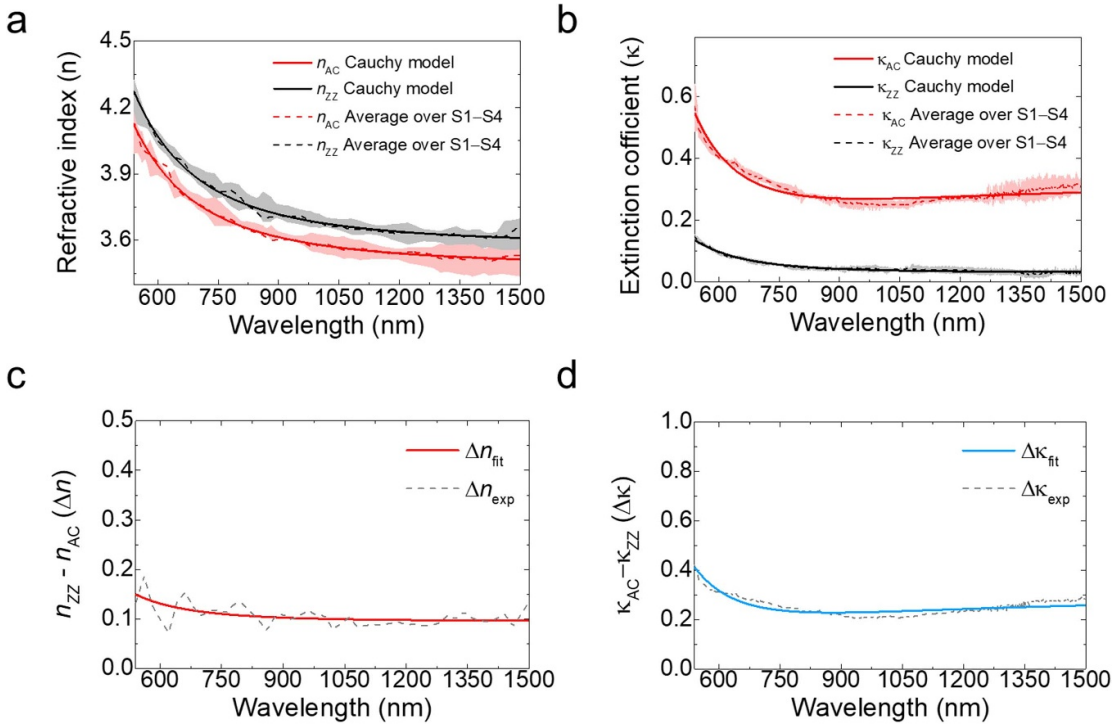

Figure 3. (a), (b) Refractive index (a) and extinction coefficient (b) dispersions for the ZZ (black) and AC (red) polarizations averaged over the results taken at the four spots S1–S4 shown as dashed lines. The color shades are the standard deviation errors. The solid lines indicate the Cauchy absorbent equation model fittings of the refractive index and extinction coefficient dispersions. (c), (d) Birefringence $\Delta n = n_{ZZ} - n_{AC}$ (c) and linear dichroism $\Delta\kappa = \kappa_{AC} - \kappa_{ZZ}$ (d) spectra. The solid lines are obtained from the Cauchy absorbent equation model, and the dashed lines are from the averaged n and κ values.

dispersions are respectively shown in figures 3(a) and (b) for both polarizations, where the averaged dispersions are plotted with dashed lines. In order to formulate the optical dispersions of BP, we adopt the Cauchy absorbent model, described by the following equations:

$$n(\lambda) = A + B\frac{10^4}{\lambda^2} + C\frac{10^9}{\lambda^4}. \quad (1)$$

$$\kappa(\lambda) = D \times 10^{-5} + E\frac{10^4}{\lambda^2} + F\frac{10^9}{\lambda^4}. \quad (2)$$

where the wavelength (λ) is in units of nm, and (A, B, C) and (D, E, F) are coefficients used for the refractive index and the extinction coefficient, respectively. As shown with solid lines in figures 3(a) and (b), the polarization-dependent A to E coefficients in table 1 well explain the anisotropic refractive index and extinction coefficient dispersions in the 540–1500 nm wavelength region. In figures 3(c) and (d), we show the wavelength dependence of the birefringence with $\Delta n = n_{ZZ} - n_{AC}$, and the linear dichroism with $\Delta\kappa = \kappa_{AC} - \kappa_{ZZ}$. While the extinction coefficient of the AC polarization is substantially larger than that of the ZZ polarization, the refractive index of the ZZ polarization is slightly larger than that of the AC polarization, with the difference varying approximately from 0.15 at 540 nm to 0.1 at 1500 nm. We note that although the optical constants were obtained from BP flakes thicker than 171 nm, the parameters remain applicable to thin samples down to 30 nm, as confirmed from the successful reproduction of the measured RC and TC spectra (see section 5 in the supporting information). We then compare the optical constants of BP in this work with other reports, as shown in section 6 in the supporting information. While the discrepancies are rather large between the reports, we stress the reliability of our result based on the self-consistency of the procedure from the precisely measured transmittance and reflectance spectra. In contrast to the positive Δn in this work, Schuster *et al* reported a negative value of Δn [21]. To investigate this discrepancy, we carried out complementary experiments using a liquid crystal phase retarder, which confirmed the positive value of Δn at 700 nm (see section 7 in the supporting information).

By providing phase retardation as a means to create circularly polarized light for valley-selective excitation in TMDCs, the birefringence of BP demonstrated in this study may be harnessed in the development of novel valleytronics elements in the form of BP/TMDC heterostructures. We now discuss the optical phase retardation and polarization manipulation in BP crystal. If a light linearly polarized by an angle θ with respect to the AC axis is incident on a BP crystal of thickness L, the transmitted electric field

Table 1. A–E coefficients for the Cauchy absorbent model to describe the refractive index dispersion of BP along the AC and *ZZ* directions.

	A	B	C	D	E	F
ZZ direction	3.57	6.79	39.99	3206	−0.521	10.26
AC direction	3.48	6.76	35.48	32 780	−10.98	50.71

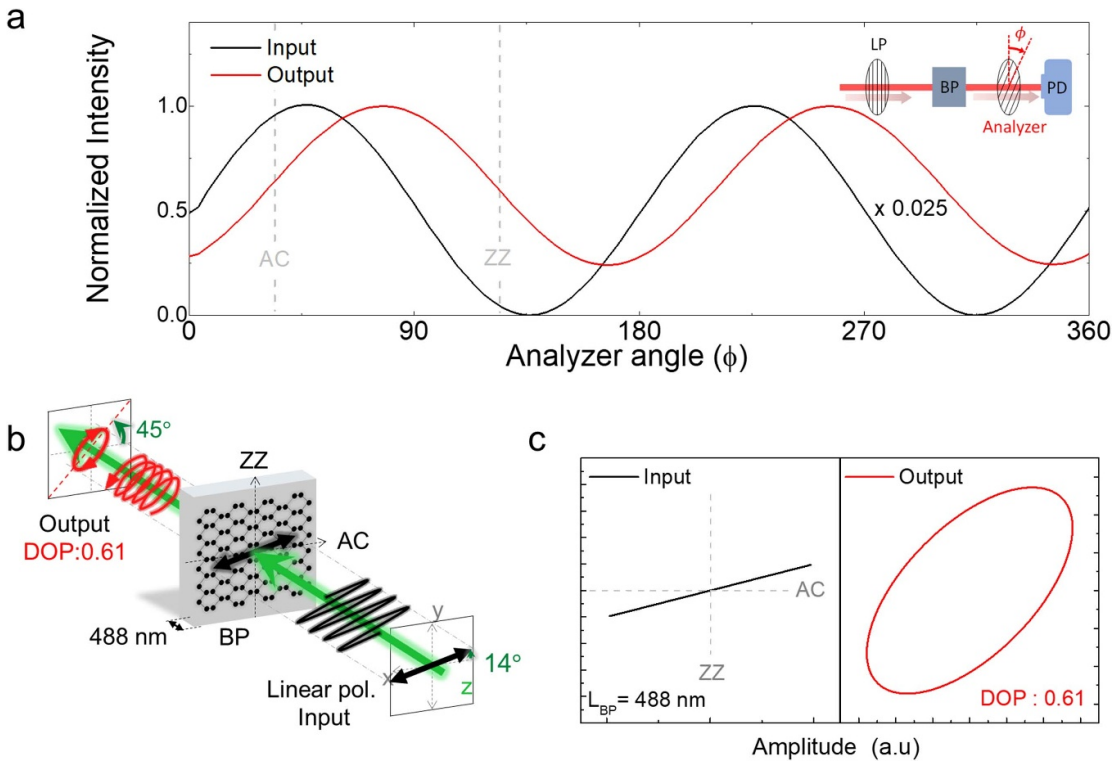

Figure 4. (a) Analyzer polarization resolved intensity of input light at 630 nm and that of the output after passing through a 488 nm thick BP flake. (b) Schematic illustration showing the polarization state change of the linear polarized light passing through the BP flake. (c) Polarization states of the linearly polarized input (left) and elliptically polarized output (right) light.

(neglecting the interfacial reflection) will be as follows [27, 28]:

$$\mathbf{E} = E_0 \cdot \cos\theta \cdot e^{-\frac{2\pi L \kappa_{AC}}{\lambda}} \cdot \cos(\omega t)\hat{x} + E_0 \cdot \sin\theta \cdot e^{-\frac{2\pi L \kappa_{ZZ}}{\lambda}} \cdot \cos(\omega t - \delta)\hat{y},$$
$$\delta \equiv (n_{ZZ} - n_{AC}) \cdot 2\pi L/\lambda$$

where E_0 is the incident electric field amplitude, ω is the frequency, and $\hat{x}$ and $\hat{y}$ are unit vectors along the AC and ZZ axis, respectively. In this case, the induced phase retardation (δ) is proportional to the birefringence multiplied by the thickness, and the amplitude is anisotropically attenuated due to the linear dichroism. But as reflections occurring at both air/BP and BP/FS interfaces add complexity, TMM analysis is required to solve the transmitted field. Recently, the material's linear dichroism has enabled BP flakes to behave as absorptive polarizers [16, 17], and the birefringence of BP has been shown to modulate the polarization state in polarized Raman spectroscopy and to induce anisotropic destructive interference [28, 29]. However, the practical operation of BP waveplates awaits further confirmation, especially in terms of modulations of the transmitted light polarization [30].

In order to demonstrate the phase retardation of the transmitted light, we investigate the polarization change occurring when a linearly polarized light passes through a BP flake. As shown in the inset of figure 4(a), the output polarization state is verified by measuring the transmitted intensity with a rotation of the analyzer (polarizer) between the photodetector and BP flake. Figure 4(a) shows how an incident linear polarization at a wavelength of 630 nm is manipulated after passing through a 488 nm thick BP flake. Here, we chose a polarization angle of 14° such that the AC and ZZ polarizations become comparable in strength after passing through the BP. Figures 4(b) and (c) show that after passing through BP, a linear polarization is elliptically polarized with an ellipticity of 0.49, and the principal axis changes from 14° to 44.5° due to the linear dichroism. This polarization change occurs primarily due to the optical phase retardation, and we find the single pass retardation to be 0.61 radian for the tested wavelength and thickness. It is

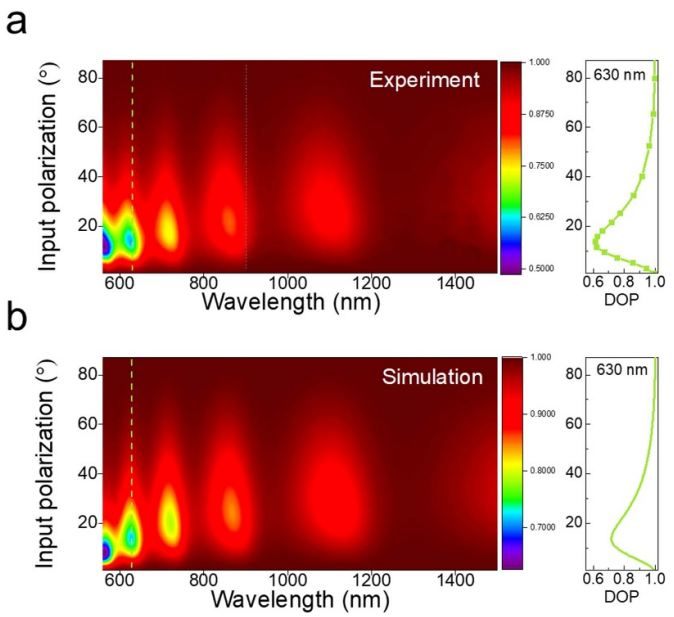

Figure 5. (a) Degree of polarization (DOP) for the light passing through a 488 nm thick BP flake as a function of wavelength and input polarization angle. (b) DOP simulated via the TMM approach with the acquired complex refractive index dispersions. The right panels of a and b show the DOPs at 630 nm as a function of input polarization angle. (c) Simulated and experimental phase retardation between the AC and ZZ axis polarization. (d) Simulated and experimental attenuation ratio between the AC and ZZ axis polarization.

noteworthy that while we observe a linear to elliptical polarization conversion of light due to the optical anisotropy, Buryakov *et al* reported on the elliptically polarized THz wave generation in BP crystals [31].

To gain further insight into the phase retardation provided by BP crystal, we investigate the output polarization with varying the wavelength and polarization angle of the input light. Here, as a measure of polarization linearity, we use the degree of polarization (DOP), defined as $(I_{max} - I_{min})/(I_{max} + I_{min})$, where I_{max} and I_{min} are the maximum and minimum intensity in analyzer angle dependence of the polarization analysis, respectively. The measured DOP contour map is shown in figure 5(a) as a function of the light wavelength and the input linear polarization in the horizontal and vertical axes, respectively. The right panel in figure 5(a) shows the DOP at a wavelength of 630 nm as a function of input polarization (see section 8 in the supporting information for the output polarization states). The contour map displays multiple low DOP regions, and we find that this signature results from thin film interference at the BP interfaces [32, 33]. The output polarization states at these low DOP conditions of the input polarization and wavelength can be found in section 9 in the supporting information. In order to verify the experimental results and thus the obtained optical constants of BP, we performed TMM simulations of the DOP using the Cauchy absorbent model of the refractive index and extinction coefficient in figure 3. A detailed description of the DOP simulation can be found in section 10 in the supporting information. The simulation results in figure 5(b) exhibit a clear resemblance in both shape and absolute magnitude with the experiment in figure 5(a), which certifies that the Cauchy absorbent model is reliable and can be applied to characterize the optical properties of BP-based photonic devices. Figures 5(c) and (d) show both the experimentally extracted and the simulated results of the phase retardation and the attenuation ratio, exhibiting an overall agreement (see section 4 in the supporting information for the simulation procedure). Here, the attenuation ratio is defined as the intensity transmittance of ZZ polarization divided by that of AC polarization, while the phase retardation is the induced phase difference between the two output polarizations. The spectral modulations in figures 5(c) and (d) indicate that thin film interference has strong effects on both the phase retardation and the anisotropic absorption in BP. It is worth noting that the attenuation ratio from BP's linear dichroism is compensatable by controlling the input polarization angle, such that low DOPs are attained at short wavelengths in spite of large attenuation ratios. Ultimately, large polarization state changes (or the low DOP regions) result from both the principal polarization axis rotation originating from the attenuation ratio and the phase retardation from the birefringence of the two axes.

The thickness of the BP layer is an important parameter in determining the phase retardation and the linear dichroism at a given wavelength. We additionally investigated the waveplate properties of a BP flake with a thickness of 379 nm. As presented in section 11 in the supporting information, the interpretation of the 488 nm thick BP applies equally

to the case of the 379 nm BP. Though we have chosen BP samples among the exfoliated flakes with a random thickness distribution, controllable BP thickness manipulation may be achieved by employing alternative fabrication methods such as layer-by-layer thinning with plasma treatment [34].

4. Conclusion

The anisotropic refractive index and absorption coefficient dispersion of BP in the visible and near-infrared region were obtained from the TMM analysis of simultaneously measured RC and TC spectra. The polarization-dependent coefficients of the Cauchy absorbent model provided in this work can be widely used in understanding the anisotropic optical properties of BP nanodevices. We demonstrated a prototype 2D material optical phase retarder, showing that a linearly polarized light is elliptically polarized with a DOP as low as 0.61 after passing through a 488 nm thick BP crystal. The results also revealed that thin film interference significantly affects both the phase retardation and polarization-sensitive absorption of BP crystal. We confirmed the reliability of the optical constants and the phase retardation in BP by successfully simulating the experimental results. By demonstrating a phase retarder application of BP crystal, we expect our work will pave the way to novel 2D material optical components used in valleytronics and photonics devices.

Data availability statement

All data that support the findings of this study are included within the article (and any supplementary files).

Acknowledgment

This research was funded by the National Research Foundation of Korea (NRF2020R1A2C1008368, NRF-2020R1A6A1A03047771).

Conflict of interest

The authors declare no competing financial interest.

ORCID iDs

Seong-Yeon Lee https://orcid.org/0000-0001-5628-2914
Ki-Ju Yee https://orcid.org/0000-0002-1076-2354

References

[1] Xia F, Wang H, Xiao D, Dubey M and Ramasubramaniam A 2014 Two-dimensional material nanophotonics *Nat. Photon.* **8** 899–907
[2] Novoselov K S, Mishchenko A, Carvalho A and Castro Neto A H 2016 2D materials and van der Waals heterostructures *Science* **353** 6298
[3] Wang Q H, Kalantar-Zadeh K, Kis A, Coleman J N and Strano M S 2012 Electronics and optoelectronics of two-dimensional transition metal dichalcogenides *Nat. Nanotechnol.* **7** 699–712
[4] Avsar A, Ochoa H, Guinea F, Özyilmaz B, van Wees B J and Vera-Marun I J 2020 Colloquium: spintronics in graphene and other two-dimensional materials *Rev. Mod. Phys.* **92** 021003
[5] Cooper D R *et al* 2012 Experimental review of graphene *ISRN Condens. Matter Phys.* **2012** 501686
[6] Caldwell J D, Aharonovich I, Cassabois G, Edgar J H, Gil B and Basov D N 2019 Photonics with hexagonal boron nitride *Nat. Rev. Mater.* **4** 552–67
[7] Xia F, Wang H and Jia Y 2014 Rediscovering black phosphorus as an anisotropic layered material for optoelectronics and electronics *Nat. Commun.* **5** 4458
[8] Wang X and Lan S 2016 Optical properties of black phosphorus *Adv. Opt. Photonics* **8** 618–55
[9] Mu X, Wang J and Sun M 2019 Two-dimensional black phosphorus: physical properties and applications *Mater. Today Phys.* **8** 92–111
[10] Abate Y, Akinwande D, Gamage S, Wang H, Snure M, Poudel N and Cronin S B 2018 Recent progress on stability and passivation of black phosphorus *Adv. Mater.* **30** 1704749
[11] Ling X, Wang H, Huang S, Xia F and Dresselhaus M S 2015 The renaissance of black phosphorus *Proc. Natl Acad. Sci. USA* **112** 4523–30
[12] Li L, Yu Y, Ye G J, Ge Q, Ou X, Wu H, Feng D, Chen X H and Zhang Y 2014 Black phosphorus field-effect transistors *Nat. Nanotechnol.* **9** 372–7
[13] Xia F, Wang H, Hwang J C M, Neto A H C and Yang L 2019 Black phosphorus and its isoelectronic materials *Nat. Rev. Phys.* **1** 306–17
[14] Wu S, Hui K S and Hui K N 2018 2D black phosphorus: from preparation to applications for electrochemical energy storage *Adv. Sci.* **5** 1700491
[15] Bullock J *et al* 2018 Polarization-resolved black phosphorus/molybdenum disulfide mid-wave infrared photodiodes with high detectivity at room temperature *Nat. Photon.* **12** 601–7
[16] Zhou F and Zhang J 2017 Polarization-independent black-phosphorus polarizer in visible regime *IEEE Photonics Techol. Lett.* **29** 1923–6
[17] Shen W, Hu C, Huo S, Sun Z, Fan G, Liu J, Sun L and Hu X 2019 Black phosphorus nano-polarizer with high extinction ratio in visible and near-infrared regime *Nanomaterials* **9** 168
[18] Schaibley J R, Yu H, Clark G, Rivera P, Ross J S, Seyler K L, Yao W and Xu X 2016 Valleytronics in 2D materials *Nat. Rev. Mater.* **1** 16055
[19] Zhu C R, Zhang K, Glazov M, Urbaszek B, Amand T, Ji Z W, Liu B L and Marie X 2014 Exciton valley dynamics probed by Kerr rotation in WSe_2 monolayers *Phys. Rev.* B **90** 161302
[20] Mao N *et al* 2016 Optical anisotropy of black phosphorus in the visible regime *J. Am. Chem. Soc.* **138** 300–5
[21] Schuster R, Trinckauf J, Habenicht C, Knupfer M and Buchner B 2015 Anisotropic particle-hole excitations in black phosphorus *Phys. Rev. Lett.* **115** 026404
[22] Jiang H, Shi H, Sun X and Gao B 2018 Optical anisotropy of few-layer black phosphorus visualized by scanning polarization modulation microscopy *ACS Photonics* **5** 2509–15
[23] Lee S-Y and Yee K-J 2021 Anisotropic generation and detection of coherent Ag phonons in black phosphorus *Nanomaterials* **11** 1202
[24] Castellanos-Gomez A, Buscema M, Molenaar R, Singh V, Janssen L, van der Zant H S J and Steele G A 2014 Deterministic transfer of two-dimensional materials by all-dry viscoelastic stamping *2D Mater.* **1** 011002

[25] Katsidis C C and Siapkas D I 2002 General transfer-matrix method for optical multilayer systems with coherent, partially coherent, and incoherent interference *Appl. Opt.* **41** 3978–87
[26] Lee S-Y, Jeong T-Y, Kim J-H, Yun S and Yee K-J 2018 Self-consistent dielectric constant determination for monolayer WSe_2 *Opt. Express* **26** 23061–8
[27] Hecht E 2002 *Optics* 4th edn 1 (San Francisco, CA: Addison-Wesley) pp 325–8
[28] Mao N, Zhang S, Wu J, Tian H, Wu J, Xu H, Peng H, Tong L and Zhang J 2018 Investigation of black phosphorus as a nano-optical polarization element by polarized Raman spectroscopy *Nano Res.* **11** 3154–63
[29] Shen W, Hu C, Huo S, Sun Z, Fan S, Liu J and Hu X 2018 Wavelength tunable polarizer based on layered black phosphorus on Si/SiO_2 substrate *Opt. Lett.* **43** 1255–8
[30] Hecht E 2002 *Optics* 4th edn 1 (San Francisco, CA: Addison-Wesley) pp 352–8
[31] Buryakov A, Zainullin F, Khusyanov D, Abdulaev D, Nozdrin V and Mishina E 2021 Generation of elliptically polarized terahertz radiation from black phosphorus crystallites *Opt. Eng.* **60** 082013
[32] Kim J, Lee J-U, Lee J, Park H J, Lee Z, Lee C and Cheong H 2015 Anomalous polarization dependence of Raman scattering and crystallographic orientation of black phosphorus *Nanoscale* **7** 18708–15
[33] Lan S, Rodrigues S, Kang L and Cai W 2016 Visualizing optical phase anisotropy in black phosphorus *ACS Photonics* **3** 1176–81
[34] Jia J, Jang S K, Lai S, Xu J, Choi Y J, Park J-H and Lee S 2015 Plasma-treated thickness-controlled two-dimensional black phosphorus and its electronic transport properties *ACS Nano* **9** 8729–36